

Synthesis and Fabrication of Multifunctional Nanocomposites: Stable Dispersions of Nanoparticles Tethered with Short, Dense and Polydisperse Polymer Brushes in Poly(methyl methacrylate)

Minhao Wong, Johannes Guenther, Luyi Sun, Janet Blümel, Riichi Nishimura, and Hung-Jue Sue*

This paper presents a melt-processable multifunctional nanocomposite material that shows highly controlled tunability in refractive index, glass transition temperature (T_g) and energy bandgap. ZnO quantum dots tethered with polymer brushes are melt-blended into the matrix polymer, giving rise to multiple functionalities in the nanocomposites. Brush–matrix polymer interactions are important in determining the ability of polymer-grafted nanoparticles to disperse in a polymer melt, of which graft density (σ), brush (N) and matrix (P) polymer lengths are the critical parameters. It is generally assumed that long polymer brushes ($N > P$) and an optimum graft density are necessary to achieve a good dispersion. Here it is demonstrated that nanoparticles tethered with short, dense and polydisperse polymer brushes via radical copolymerization can exhibit a stable, fine dispersion in the polymer melt. The quality of the dispersion of the nanoparticles is characterized by measuring physical properties that are sensitive to the state of the dispersion. This synthesis method presents a general approach for the inexpensive and high-throughput fabrication of high quality, melt-blendable nanocomposites that incorporate functional nanoparticles, paving the way for wider application of high performance nanocomposites.

1. Introduction

Inorganic nanoparticles tethered with polymer brushes are an important class of materials with unique properties that are dependent on the nature of the brushes. They form extremely stable Pickering emulsions^[1] and have been shown to self-assemble into 2D ordered structures.^[2] Recent progress suggests that colloids comprised of such nanoparticles are also promising candidates as stimuli-responsive materials^[3] that respond to thermal^[1,4] and pH^[5] stimuli, opening up new vistas for applications. The use of functional inorganic nanoparticles such as titanium dioxide,^[6] silica,^[7,8] aluminium oxide,^[9] iron oxide,^[10] zinc oxide,^[11] cadmium selenide,^[12] gold^[13] and others in nanocomposites is a promising approach to introduce new functionalities to a polymer such as tunable refractive index, magnetism, surface hardness, UV absorption, etc. However, aggregation of nanoparticles

is commonly encountered, leading to unsatisfactory performance of nanocomposites and frustrating efforts to utilize functional nanoparticles in applications. Many approaches exist to alleviate the aggregation problem. Amongst them, the polymer brush/nanoparticle system remains the most promising. This is due to the fact that numerous examples of stable and highly dispersed nanoparticles in nanocomposites already exist. Such stable dispersions work through the “wetting-dewetting” phenomenon of polymer brushes. Wetting of the brush by free polymer chains ensures a good dispersion while dewetting of the brush, forming the so-called “dry brush”, encourages aggregation of the nanoparticles. Wetting occurs when free polymers mix freely with the grafted polymer brush; conversely, dewetting occurs when free polymers do not penetrate into the brush and as a consequence, no mixing happens. In the absence of enthalpic effects, i.e. interactions due to different brush-matrix chemical structures, and other effects such as magnetic or electrostatic attractions, the dispersion of polymer-grafted nanoparticles in a chemically identical matrix is determined by entropic factors. Existing studies done on polymer brushes on flat^[14]

Prof. H.-J. Sue
Texas A&M University
Department of Mechanical Engineering
Polymer Technology Center
College Station, TX 77843-3123, USA
E-mail: hjsue@tamu.edu

M. Wong
Texas A&M University
Materials Science and Engineering Program
Polymer Technology Center
College Station, TX 77843-3123, USA

J. Guenther, Prof. J. Blümel
Department of Chemistry
Texas A&M University, College Station, TX 77842, USA

Prof. L. Sun
Texas State University—San Marcos
Department of Chemistry and Biochemistry
601 University Dr, San Marcos, TX 78666, USA

R. Nishimura
Kaneka Corporation
Frontier Materials Development Laboratories
5-1-1, Torikai-Nishi, Settsu, Osaka 566-0072, Japan

DOI: 10.1002/adfm.201200083



and curved surfaces^[15,16] identified several parameters, namely matrix polymer degree of polymerization P , brush polymer degree of polymerization N and graft density σ , that are critical in determining the formation of a stable dispersion. There is an entropic penalty associated with stretching out a coiled chain when matrix polymer and brush polymer interpenetrate. A longer brush polymer suffers less penalty to stretch out, thus for $N > P$ brush-polymer interpenetration is favorable, which leads to wetting of the brush and good dispersion. Conversely, when $P > N$, dewetting of the brush occurs, which results in poor dispersion. Hasegawa *et al.*^[15] examined in detail the effect of graft density on the aggregation phenomenon in polymer/particle mixtures and concluded that when $P \sim N$ an optimal graft density σ_c can be estimated by $\sigma_c \approx N^{-1/2}a^{-2}$, where a is the monomer size. Experimental studies have generally confirmed these predictions in both planar and colloidal brushes.^[10,13,17–19] Recently, it has been recognized that surface curvature plays a huge role in the dispersion of nanoparticles^[20,21] to account for the fact that good dispersion is still observed in cases where $P > N$.^[10]

Nevertheless, despite being such a well-studied field, an explosion of polymer brush-nanoparticles being used in technological applications has yet to be seen, with one notable exception of nylon-clay nanohybrids.^[22] A few reasons may be suggested to explain such paucity of diverse applications; complex synthesis, specificity of surfactant molecules, limited applicability of synthesis methods for different polymer/nanoparticle systems, etc. It is the opinion of the authors that one of the most important limiting factors is the lack of a synthesis method that can be adapted easily to commonly used polymer processing techniques, most notably melt-processing. The success of the nylon-clay nanohybrids can in huge part be attributed to the melt-processability of the material. The primary objective of this paper is thus to present a synthesis method that is generally applicable to diverse nanoparticle/polymer combinations and yields a product that is amenable to melt-processing methods. This means that the nanoparticle remains stable and finely dispersed during melt-processing without detrimental effects to its functional properties. A corollary to the aforesaid goal is demonstrating that the nanocomposites thus fabricated exhibit multiple new functionalities as a result of the fine dispersion of inorganic nanoparticles. The mechanisms that allow the polymer brush tethered nanoparticles to maintain their dispersion in the melt phase will also be discussed in detail.

2. Polymer-Grafted Nanoparticles

We have prepared PMMA-grafted zinc oxide (ZnO) nanoparticles *via* a free radical copolymerization process according to the reaction scheme shown in Figure 1a. The ZnO nanoparticles are synthesized, followed by silanization. The nature of the silane anchored to the ZnO surface is probed using ²⁹Si solid-state CP/MAS NMR.^[23] The identification of the silane-ZnO bonding mode follows the classification by Veeman *et al.*,^[24,25] which is illustrated in Figure 1b. The silane bonding type T⁰ can be unequivocally assigned to both samples based on the peaks at −34.1 ppm and −33.5 ppm for Batch 1 and Batch 2, respectively (Figure 1c). The absence of any peaks in the area of −60 to

−68 ppm rules out T² surface-bonding^[25] and Q³ species,^[24] and therewith the formation of multiple cross-linked silane layers on the surface, or a gel process taking place in solution. Furthermore, the absence of any signals in the region from −42 to −46 ppm, which would indicate T¹ surface-bound species, proves unequivocally that the silane molecules do not cross-link on the surface. Therefore, we conclude that all silane molecules fall into the T⁰ category and are exclusively bound to the ZnO surface by three Si-O-Zn bridges. The silanized ZnO nanoparticles were then copolymerized in the presence of methyl methacrylate (MMA) monomer in *N,N*-dimethylformamide (DMF) solution in order to form PMMA-grafted ZnO nanoparticles. Transmission electron microscopy (Figure 2a) shows that the nanoparticles exhibit a narrow size distribution of 3.4 ± 0.8 nm in diameter^[26] according to the histogram of particle diameters from a total of 150 nanoparticles measured over several TEM images (Figure 2b). In contrast to the more common method of grafting polymers using surface-initiated polymerization techniques,^[27] this approach allows us to tether polydisperse polymer brushes with a polydispersity index (PDI) ≈ 2 , closely matching the PDI of the matrix polymer used in subsequent melt-blending. In fact, a bimodal distribution is detected (Supporting Figure S1), where the major peak is found to have $M_n = 9.5$ kgmol^{−1}, $M_w = 21$ kgmol^{−1}, PDI = 2.2 and the minor peak is found to have $M_n = 0.5$ kgmol^{−1}, $M_w = 0.6$ kgmol^{−1}, PDI = 1.2. By integration of the area under the peaks, the mass ratio of major to minor population is found to be 16: 1. Similar copolymerization procedures have been utilized to synthesize well-dispersed nanocomposites with high nanoparticle concentrations.^[28] Nevertheless, a major drawback of this method has been that the nanocomposites synthesized are not redispersible in a solvent or polymer melt due to the formation of cross-links with the nanoparticles acting as cross-linking nodes during polymerization. This limitation has now been overcome by controlling the concentration of the nanoparticles in solution to prevent the formation of cross-links.

A series of experiments was conducted to determine the optimal conditions for polymerization in the presence of silanized ZnO. The experimental conditions are presented in Table 1. Reaction temperature, ZnO concentration, ZnO/MMA ratio and silane species were varied. On the basis of the maximum conversion of monomer, the higher temperature reactions 6 and 7 were determined as optimal. Products from reactions 6 and 7 were used in the subsequent preparation of nanocomposites in this paper and identified as Batch 1 and Batch 2, respectively. We found that a higher concentration of ZnO (reaction 3) resulted in a gelatinous solid that was neither redispersible in toluene nor melt-processable. This suggests that cross-linking of the polymer chains occurred during polymerization with the densely grafted ZnO acting as nodes. Increasing ZnO concentration relative to monomer concentration (reaction 5) depressed the maximum conversion of monomer, indicating that the ZnO/MMA ratio exerts a strong effect on the kinetics of polymerization. Finally, ZnO functionalized by phenyltrimethoxysilane (PTMS), which lacked a vinyl group, was used instead of 3-(trimethoxysilyl)propyl methacrylate (TSMA) in reaction 2. Surprisingly, the resulting product was redispersible in toluene yielding a transparent solution, despite the absence of covalent linkage between polymer and ZnO. However, the

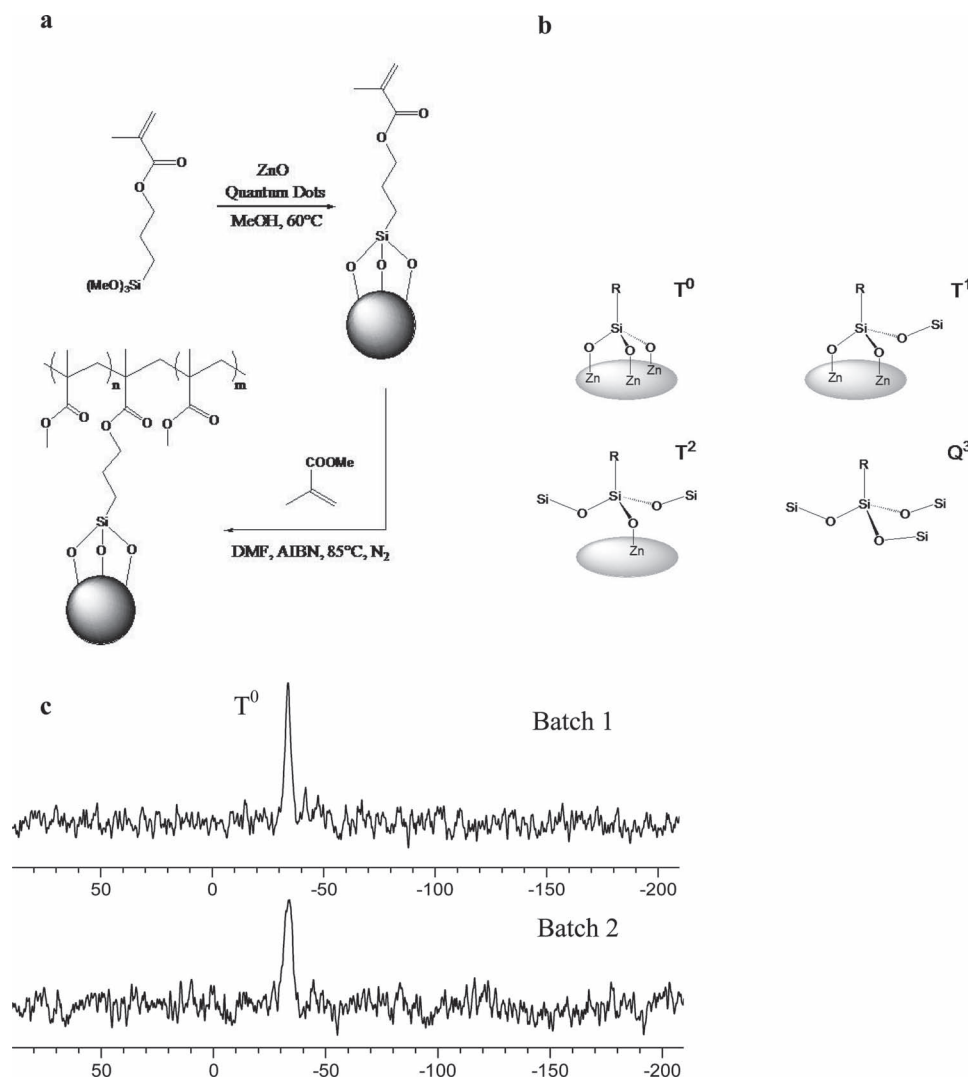


Figure 1. (a) Reaction scheme for the preparation of PMMA-grafted ZnO. (b) Classification of silane bonding types T⁰, T¹, T², and Q³.^[23,24] (c) The ²⁹Si solid-state NMR spectra of two PMMA-grafted ZnO batches. The ²⁹Si signals appear at chemical shifts of $\delta = -34.1$ and $\delta = -33.5$ ppm for Batch 1 and Batch 2, respectively.

dried product did not form a transparent nanocomposite after melt-processing, due to the presence of aggregates in the polymer matrix, demonstrating that the grafting of the polymer through a covalent bond is necessary in achieving a fine dispersion of nanoparticles in the melt phase.

3. Fine, Stable Dispersion of Nanoparticles

The resultant polymer-grafted nanoparticles are fully melt-blendable and resistant to aggregation even with extended annealing above the glass transition temperature T_g . We were able to produce melt-blended nanocomposites that are highly transparent, as illustrated by a nanocomposite containing 9.87 wt% ZnO, formed into a 0.2 mm thick sheet, shown in Figure 2c. The transparent sheet showed no preferential absorption of color, resulting in a high quality, near colorless appearance. The nanocomposites exhibit surprising tunability

of T_g , refractive index and energy bandgap. To the best of our knowledge, this is the first example of a melt-blendable nanocomposite exhibiting such multifunctional properties. Nanocomposites with varying ZnO concentrations are prepared by melt-blending proportional amounts of PMMA-grafted ZnO with a commercial grade PMMA ($M_n = 65$ kgmol⁻¹, $M_w = 146$ kgmol⁻¹, PDI = 2.2) in a batchmixer, after which the melt-blended nanocomposites are injection molded into bars. The dispersion stability is investigated by comparing the dispersion of the nanofillers of injection molded nanocomposites with nanocomposites that are subsequently annealed for 5 days at 160 °C, which is well above the T_g values of the nanocomposites.

The state of the dispersion is monitored using transmission electron microscopy (TEM), UV-Vis spectroscopy, refractive index analysis using a prism coupler, and T_g characterization by dynamic mechanical analysis (DMA) and differential scanning calorimetry (DSC). From the TEM results (Figure 3), it is

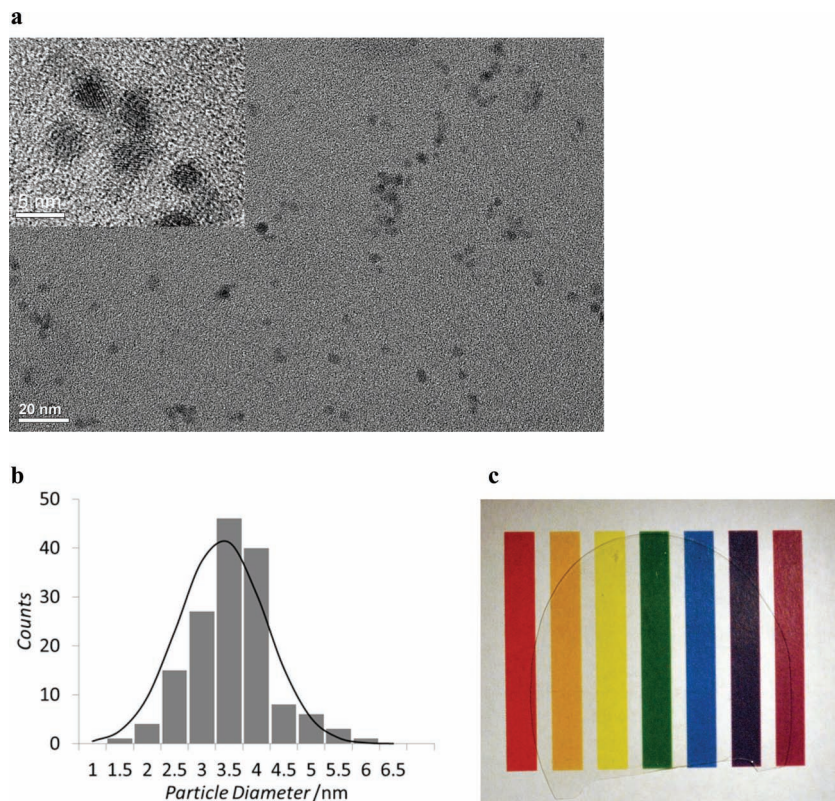


Figure 2. (a) TEM image of PMMA-grafted ZnO dispersed by melt blending in neat PMMA, (inset) HRTEM of PMMA-grafted quantum dots. (b) Histogram of particle diameters of 150 nanoparticles yielding an average diameter of 3.4 ± 0.8 nm. (c) Photographic image of a nanocomposite sheet (thickness = 0.20 mm) formed by melt blending of PMMA-grafted ZnO with neat PMMA followed by annealing, ZnO = 9.81% by weight, demonstrating the quality of transparency with no preferential absorption of a particular color in the visible range.

observed that the dispersion of the nanoparticles shows only little change before and after annealing. Significantly, in contrast to previous studies^[19,29] we do not observe any aggregation, self-assembly of nanoparticles into secondary structures or segregation of nanoparticles to a free surface after annealing. In the

pre-annealed samples (Figure 3, left column), there appear to be clusters of ZnO nanoparticles distributed throughout, but detailed analysis reveals that the nanoparticles remain individually separated and the tunability of T_g does not seem to be affected. The linearity of the relation of T_g to ZnO concentration has been verified independently through DMA and DSC. For the sake of brevity, detailed arguments supporting this conclusion have been published elsewhere (Wong *et al.*^[30]) and will not be repeated here. The electron micrographs of the annealed nanocomposites (Figure 3, right column) show that the nanoparticles remain well-dispersed throughout the matrix with an apparent improvement of homogeneity due to fewer occurrences of the clusters.

3.1. Tunability of Energy Bandgap

UV-Vis spectroscopy (Figure 4a) of nanocomposites that were annealed at 160 °C for 5 days and subsequently pressed into sheets (~0.20 mm thick) shows transmission levels close to neat PMMA (~90%). However, at higher ZnO loadings, weak absorption around 400 to 500 nm leads to a very slight yellowish tinged appearance of the nanocomposite. The nanocomposite sheets absorbed all wavelengths shorter than 370 nm. The dependence of the absorption wavelength of the nanocomposite on the quantum dot concentration is due to the quantum coupling of exciton states in closely spaced quantum dots. The formation of delocalized energy bands as the quantum dots approach each other lowers the energy of the radiation absorbed,^[31] in effect decreasing the energy bandgap of the quantum dots. This phenomenon is clearly observed in the absorption spectra

Table 1. Experimental conditions for the grafting of PMMA to ZnO.

S/N	Silane ^{a)}	Temperature (°C)	Conc. (% wt)	ZnO			MMA		ZnO/MMA			Total Volume of Reaction (ml)	Maximum Conversion ^{b)} (%)	Redispersible in toluene?
				Conc. [M]	Conc. (% vol)	Conc. (% wt)	Conc. [M]	Conc. (% vol)	wt/wt	[M]/[M]	vol/vol			
1	TSMA	65	1.60	0.19	0.27	9.07	0.86	9.13	0.18	0.22	0.030	269	66.7	Yes
2	PTMS	65	1.60	0.19	0.27	9.07	0.86	9.14	0.18	0.22	0.030	269	64.9	Yes
3	TSMA	65	3.99	0.46	0.67	22.73	2.14	22.82	0.18	0.22	0.029	100	81.8	No
4	TSMA	85	1.61	0.19	0.27	9.10	0.86	9.14	0.18	0.22	0.030	215	76.8	Yes
5	TSMA	85	1.60	0.19	0.27	3.74	0.35	3.77	0.43	0.53	0.072	215	60.2	Yes
6	TSMA	85	1.80	0.21	0.30	9.12	0.86	9.19	0.20	0.24	0.033	1912	87.3	Yes
7	TSMA	85	1.80	0.21	0.30	9.11	0.86	9.19	0.20	0.24	0.033	2256	88.4	Yes

^{a)}TSMA = 3-(trimethoxysilyl)propylmethacrylate, PTMS = phenyltrimethoxysilane; ^{b)}Maximum conversion of monomer determined by weighing solid content of samples at end of reaction; The initiator AIBN was fixed at 2% wt of MMA. All experiments were carried out in DMF solution under nitrogen atmosphere for 5 h.

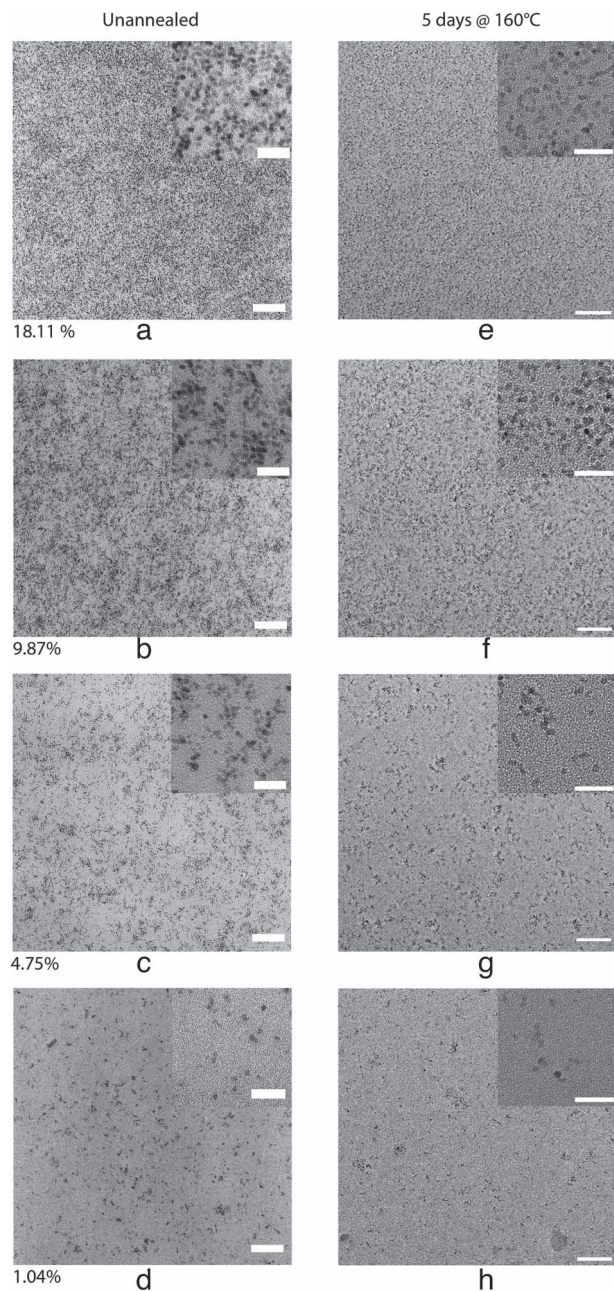


Figure 3. TEM images of unannealed (Batch 1) nanocomposites (left column) and nanocomposites annealed at 160 °C for 5 days (right column). Brush polymer $M_n = 9.5 \text{ kgmol}^{-1}$, $M_w = 21 \text{ kgmol}^{-1}$, PDI = 2.2, matrix polymer $M_n = 65 \text{ kgmol}^{-1}$, $M_w = 146 \text{ kgmol}^{-1}$, PDI = 2.2. Scale bars represent 100 nm and 25 nm for the main and inset images, respectively. ZnO content is indicated at the bottom of the images in the left column.

(Figure 4b) of our nanocomposites where the absorption edge red-shifts from 3.51 eV to 3.41 eV from lowest to highest ZnO concentration, respectively. PMMA-g-ZnO dispersed in chloroform is used as a model for isolated ZnO quantum dots. The absorption red-shifts of the nanocomposites are referenced to the absorption energy of isolated ZnO quantum dots and plotted against the interparticle distance h_p (see Supporting

Info), which, surprisingly, showed a linear dependence of energy red-shift to h_p (Figure 4c). Although highly concentrated quantum dots in polymer matrices have been known to show red-shifts in the energy absorbed,^[26,32] this is the first known report of such linear dependence and may be a result of the uniform dispersion. This explanation is consistent with the observation of homogeneous distribution of the nanoparticles in the TEM images (Figure 3).

3.2. Tunability of T_g

The nanocomposites showed a tunability of T_g when the ZnO content was varied; T_g , as measured by DSC, increased linearly with the ZnO concentration (Figure 5a). This phenomenon was reproducibly observed in two different batches of nanocomposites and also in the T_g measured by DMA. The T_g values of the nanocomposites were found to be a function of h_p , in excellent agreement with the Long-Lequeux model based on the percolation of slow dynamic domains. A detailed analysis of this phenomenon has already been reported elsewhere (Wong *et al.*^[30]) and will not be elaborated here. The presence of nanoparticles has been found to have a significant impact on the T_g trend,^[33] while linear T_g dependence has been observed only in the absence of particle aggregation.^[34]

3.3. Tunability of Refractive Index

To obtain an accurate analysis of the refractive index, the volume fractions of all the components were considered. By plotting the ZnO weight against the reciprocal of the nanocomposite density, the slope of this graph can be used to evaluate the effective density of the silane in the nanocomposite (refer to supporting information). We found that the effective density of the silane in Batch 1 and Batch 2 nanocomposites are 1.094 gcm^{-3} and 1.160 gcm^{-3} , respectively. The difference in densities between the silane and PMMA (1.180 gcm^{-3}) is less than 10%, thus justifying the assumption that the volume contribution from the silane is small and negligible. In Figure 5b (inset), the volume fraction of ZnO QDs is plotted against its weight fraction. Subsequently, the refractive index of the nanocomposite is plotted against the ZnO volume fraction and compared with known physical models. The refractive indices of mixtures are described by the Lorentz-Lorenz formula (Equation S4) if the mixing occurs at the molecular level.^[35] The refractive index of a mixture with mesoscale level mixing requires the use of other forms of effective medium theories to describe the contribution of nanosized inclusions in a host medium,^[36] of which the Maxwell-Garnett (Equation S5) and Bruggeman (Equation S6) theories are of particular relevance here. The Maxwell-Garnett model assumes that monodispersed, nanosized spheres are dispersed in a host medium, while the Bruggeman theory describes polydispersed spheres and intermixing phases in a host medium. In the calculations of the refractive index of nanocomposites, the refractive index of bulk ZnO was taken as 2.021 at 589.3 nm,^[37] and we assumed that the refractive index of grafted silane is very similar to PMMA due to their

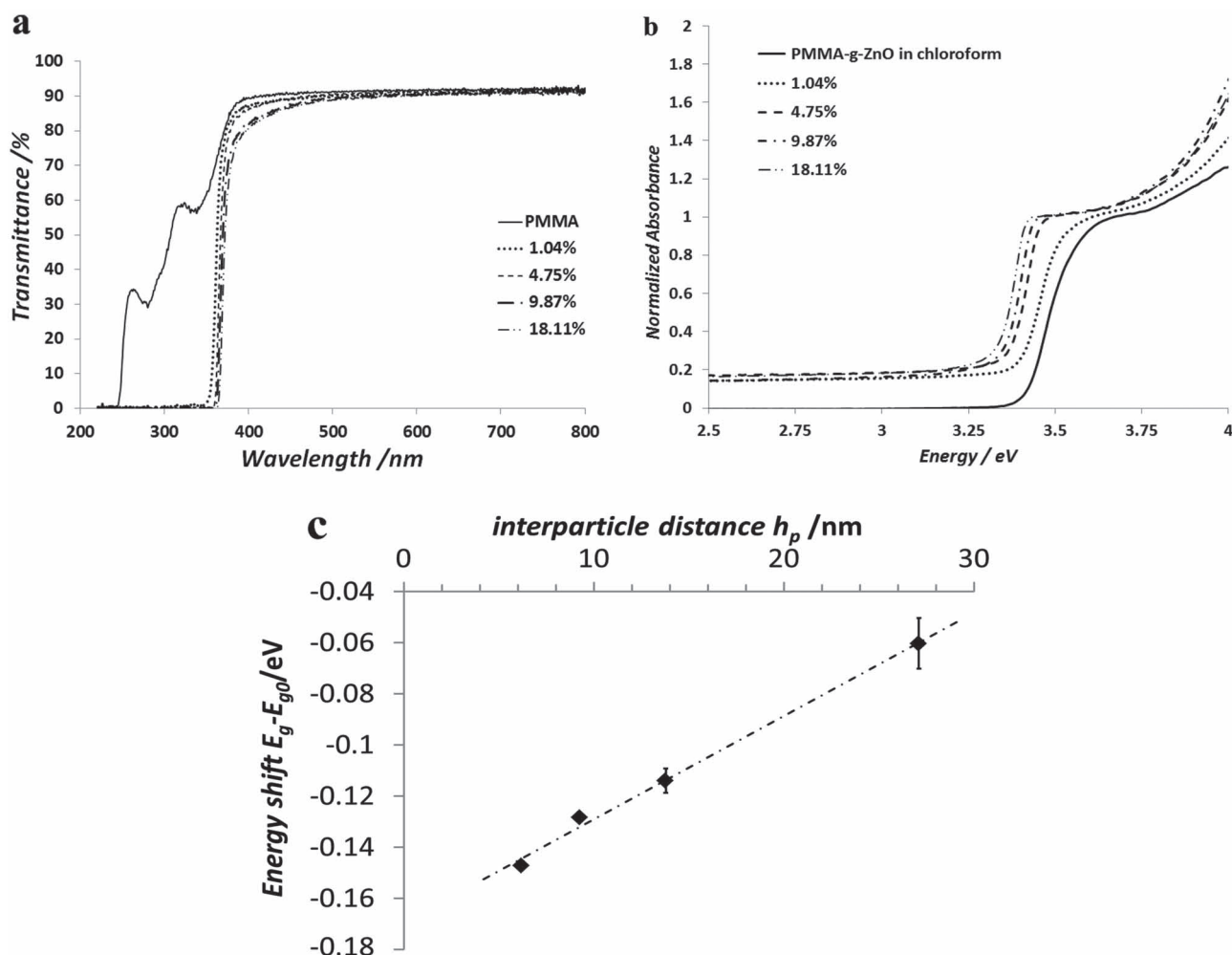


Figure 4. (a) UV-Vis transmission of annealed nanocomposite sheets at different ZnO loadings showing high transmission levels close to neat PMMA. The absorption edge red-shifts as ZnO concentration increases. (b) Normalized absorption spectra of nanocomposites compared to isolated PMMA-g-ZnO in chloroform solution. The absorption was normalized to the absorbance at the knee of the trace. (c) Magnitude of energy red-shift of ZnO increases linearly with shorter interparticle distance h_p . Interparticle distances (nm) are 27.1, 13.8, 9.3 and 6.2 for nanocomposites of 1.04%, 4.75%, 9.87% and 18.11% ZnO by weight, respectively.

similar chemical structures. Although the refractive index of the liquid silane (1.431) is significantly different ($\sim 4\%$, a large difference for refractive indices) compared to PMMA (1.4912), the absence of any true silane “liquid” in the nanocomposite and the grafting of the silane to PMMA chains should render its polarizability and therefore refractive index close to that of PMMA. The refractive index of the nanocomposite was found to increase linearly with the ZnO concentration (Figure 5b). The Lorentz-Lorenz formula consistently underestimates the measured refractive indices of the nanocomposites, suggesting that the nanoparticles have not achieved the level of homogeneity observed in other studies.^[38] By contrast, both the Maxwell-Garnett and Bruggeman theories were in excellent agreement with the experimental data. It is noteworthy that very close agreement between theory and experiment was achieved without any empirical adjustment. By comparing the predictions from different models, we see a measurable change in the refractive index with different degrees of dispersion of the nanoparticles. These results suggest that further studies of the

impact of the dispersion on the refractive index may yield a quantitative measure of the state of dispersion.

4. Nature of Polymer Brushes

It is worthwhile to investigate the reasons for the stable dispersion of the PMMA-grafted ZnO. If the grafting degree g_d , which is the weight ratio between the grafted species to the particle, particle diameter D , particle density ρ and molecular weight of the grafted species M_g are known, the graft density σ can be calculated by the following equation

$$\sigma = \frac{g_d D \rho N_A}{6 M_g} \quad (1)$$

where N_A is Avogadro's number.

Based on elemental analysis, the graft density of silane on ZnO is found to be 1.05 molecules per nm^2 . From the GPC results, using $M_n = 9.5 \text{ kgmol}^{-1}$, $g_d = 4.44$ (organic

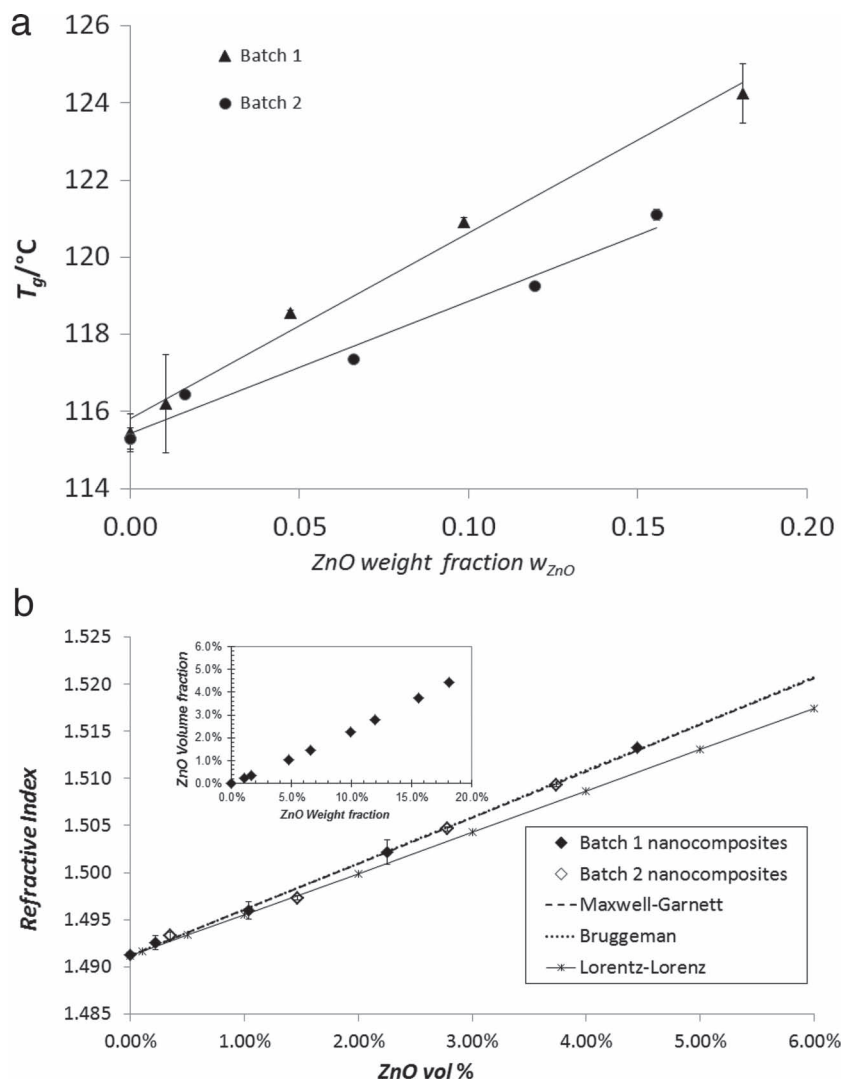


Figure 5. (a) Linear dependence of T_g to ZnO weight fraction demonstrates tunability of T_g by varying ZnO loading. Error bars indicate standard deviation. (b) Plot of refractive index against ZnO vol%. Theoretical predictions from Maxwell-Garnett, Bruggeman and Lorentz-Lorenz models are plotted for comparison. Error bars indicate standard deviation. (inset) ZnO volume fraction plotted against weight fraction.

weight = 81.6%, inorganic weight = 18.4%), $D = 3.4$ nm and $\rho = 5.606$ gcm $^{-3}$, the graft density for the major PMMA population is found to be 0.89 chains per nm 2 . We note that the choice of M_n over M_w to calculate graft density is justified as it is closer to the chains with the most probable molecular weight in the molecular weight distribution. This result suggests that the grafted polymer chains did not occupy all available grafting sites. In spite of this, a very densely grafted nanoparticle is produced that is comparable to those reported in the literature using surface-initiated polymerization methods.^[1,10,39] The intriguing question is whether the minor polymer population is grafted to the nanoparticles or exists as free chains. Nevertheless, due to its extremely short chain length and low concentration, it is reasonable to assume that the minor population plays a small role in the brush-matrix interaction.

Based on the above results, the reduced tethered density $\Sigma = \sigma \pi R_g^2$ was found to be ~ 21 , assuming the unperturbed radius of gyration $R_g = 2.76$ nm (according to Tamai *et al.*^[40] for $M_w = 10.9$ kgmol $^{-1}$). This implies that the grafted polymer forms an extended stretched-out brush if it consists of end-tethered chains, according to Brittain and Minko.^[41] To verify that a dense stretched-out brush was indeed formed, the particle size was analyzed by dynamic light scattering (DLS) and atomic force microscopy (AFM). Five aliquots of PMMA-grafted ZnO dispersed in acetone at a concentration of $\sim 10^{-3}$ g mL $^{-1}$ were prepared and measured by DLS at 25 °C. The Z-average diameter was reported as 37.8 ± 0.80 nm with a polydispersity of 0.121 ± 0.029 , CONTIN derived intensity-weighted distribution peak average was 46.6 ± 2.1 nm. A drop of acetone solution of PMMA-grafted ZnO ($\sim 10^{-5}$ g mL $^{-1}$) was deposited on a Si wafer cleaned by piranha solution (3:1 37% sulfuric acid and 30% hydrogen peroxide mixture; note: piranha solution is highly corrosive and exothermic when mixed with organic matter, proper safety precautions should be taken during handling), and subsequently dried at 70 °C for 3 days before scanning with AFM. Figure 6a illustrates the height image of a $2 \mu\text{m} \times 2 \mu\text{m}$ area, respectively. The images revealed a uniform distribution of sparsely spaced nanoparticles that was conducive for particle analysis. Particle diameters from a $10 \mu\text{m} \times 10 \mu\text{m}$ area (not shown) were measured and plotted as a histogram in Figure 6b. A total of 150 nanoparticles was measured giving an average diameter of 33.8 ± 8.0 nm after tip convolution has been corrected for. Figure 6c illustrates a high resolution 3D image that reveals the hemispherical shape of the polymer brush. The lateral dimensions of the particles were used to estimate brush height as it is known

that soft polymer brushes can be compressed by the AFM tip, thus resulting in an underestimation of the brush height.^[7,42] The brush height can be determined by subtracting the ZnO quantum dot radius (1.7 nm) from the measured nanoparticle radii. Thus the brush height is 17.3 nm, 22.0 nm and 15.3 nm as derived from the z-average, intensity-weighted distribution peak average and AFM diameters, respectively. We note that the z-average value is very close to the value obtained by AFM, providing further confirmation of the validity of the data. The theoretical stretched-out brush height is estimated by assuming an sp^3 bond angle of 109.5° between two consecutive C–C bonds (bond length = 0.154 nm) for a polymer chain fully extended in a line; the calculated values are 23.77 nm and 52.19 nm for a PMMA chain of $M_n = 9.5$ kgmol $^{-1}$ and $M_w = 21$ kgmol $^{-1}$, respectively. By this analysis, it is observed that the brush heights measured by both DLS and AFM are closer in value

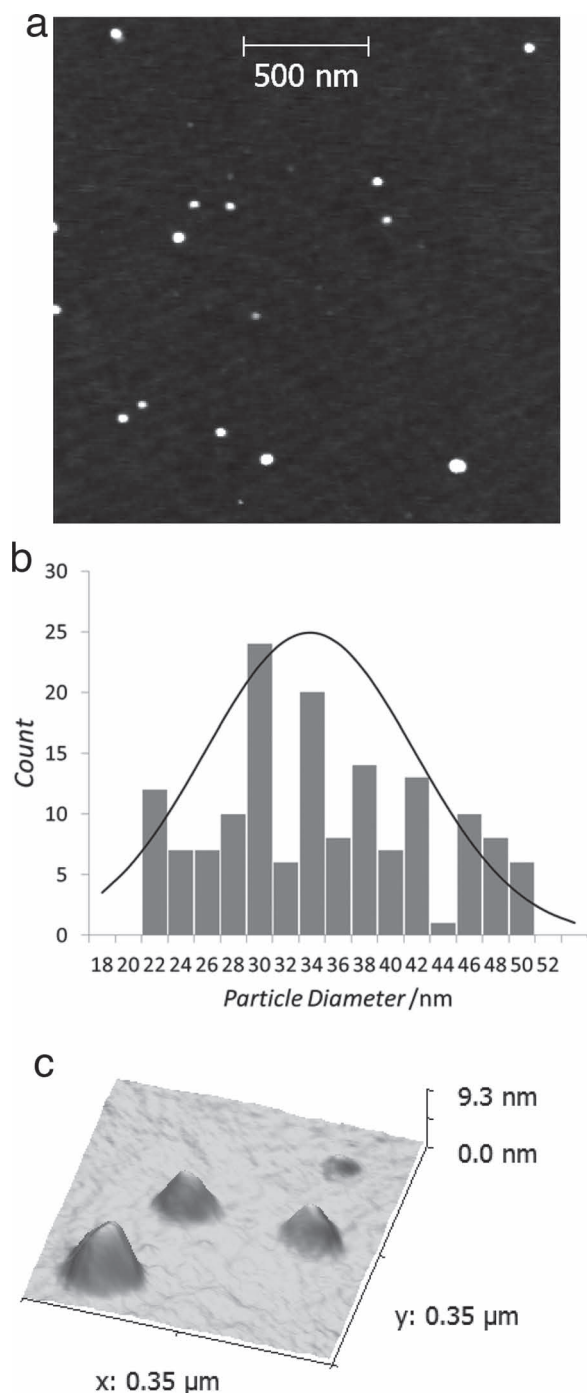


Figure 6. (a) AFM height image of a $2\ \mu\text{m} \times 2\ \mu\text{m}$ area of PMMA-grafted ZnO deposited on Si wafer. (b) Histogram of particle diameters measured from a total of 150 particles over a $10\ \mu\text{m} \times 10\ \mu\text{m}$ area (not shown) yielding an average of $33.8 \pm 8.0\ \text{nm}$. (c) High resolution 3D height profile of nanoparticles. Nanoparticles were dried at $70\ ^\circ\text{C}$ for 3 days before scanning.

to the expected brush height of a fully extended chain with a molecular weight equivalent to M_n . Unfortunately, this does not allow us to conclude if tethering occurs mainly in the middle or the end of the chain due to the distribution of polymer chain

lengths (we expect the AFM measured brush height tethered at the chain center in an ideal monodisperse brush to be half of the fully extended chain). However, the brush heights as measured by DLS are similar to the values reported by Dukes *et al.*^[39] for polystyrene (which has a similar monomer size as PMMA) brushes of comparable M_w , suggesting that the brush is in the concentrated polymer brush regime, which further implies that the polymer brush is indeed densely packed and extended.

5. Physics of Stable, Fine Nanoparticle Dispersion

Having established that a dense, extended brush was achieved, we can proceed to explain the stability of the nanoparticles. Although Leibler's analysis^[16] is applicable to colloidal particles that are much larger than the unperturbed R_g of the brush, it ignores surface curvature effects that allow for a more open brush configuration similar to a star polymer,^[43] and hence performs poorly in explaining observations of stable dispersions of small nanoparticles when $P > N$.^[10,18] Surface curvature effects were discussed in detail by Trombly and Ganesan,^[21] who identified two parameters characterizing the surface curvature of the system; R/R_g , the ratio of the particle radius to unperturbed radius of gyration of the brush and H_b/R , the ratio of the brush height to particle radius. Simulation studies concluded that at high curvatures $R/R_g = 1$, matrix-brush interpenetration is greater, attractive potential between nanoparticles is decreased and polymer brush is compressed more deeply. Significantly, lower R/R_g values increase matrix-brush interpenetration even when the matrix chain length is larger than grafted chain length. These results also correlate with that at the limit of high curvature $H_b/R \gg 1$, where increased matrix-brush interpenetration is observed. It was also found that the effect of high graft density in inducing dewetting of the polymer brush is less important for highly curved nanoparticles. The overall effect of high curvature is the better dispersion of the nanoparticles. In the current brush-nanoparticle system, we find that $R/R_g = 0.6$ and H_b/R ranges from 10 to 22 depending on the particular brush height value employed, thus satisfying the high surface curvature criteria.

To date, little effort has been made in studying the impact of brush polydispersity on nanoparticle dispersion. However, it was found through simulation by Smith and Bedrov^[44] that at $P/N = 14$, good dispersion of monodisperse brush tethered nanoparticle is still possible provided that brush density is low. It was suggested in the same study that in the case of high brush density, a combination of long and very short brushes would result in good nanoparticle dispersions. The long brushes would facilitate brush-matrix interpenetration, while the very short brushes would prevent direct contact between nanoparticles. These predictions are consistent with our observations as the broad PDI (~ 2.2) of our grafted PMMA includes a substantial fraction of long and very short polymer chains. We note that $P/N = 7$ for our polymer tethered nanoparticles, by contrast, poor dispersion occurs when P/N is greater than 4 in the polystyrene (PS) nanocomposites of 13.4 nm silica nanoparticles tethered by a monodisperse brush ($M_n = 24\ \text{kgmol}^{-1}$, PDI = 1.3) dispersed in a polydisperse matrix ($M_n = 140\ \text{kgmol}^{-1}$, PDI = 2) studied by Chevigny *et al.*^[18]

Finally, it could be argued that the observed stability is a kinetic effect due to high shear during melt-blending, which can break up aggregates to form a more homogeneous dispersion—an effect absent in a nanocomposite prepared via solution methods. However, the nanoparticles remain finely dispersed even after prolonged annealing. Although we cannot rule out kinetic effects definitively in our experiments, a review of the results of Akcora *et al.*^[19] who employed similar annealing steps in comparable nanocomposites resulted in complex anisotropic aggregates, in contrast to the extraordinary stability of our nanoparticles. Since any stabilization provided by the kinetic effect would be lost after such a prolonged period in the melt phase, this comparison supports the assertion that the stability of our nanoparticles can be accounted for based on the aforementioned thermodynamic arguments alone.

6. Conclusions

We presented a method of preparing melt-processable nanoparticle–nanocomposites exhibiting tunable multifunctional properties as a result of their fine dispersion state. This method features several unique advantages that allow for the exploitation of useful functional properties that can be brought about only by the incorporation of inorganic nanoparticles into a polymer. The key findings can be summarized as follows:

- (1) The grafting of polymers onto inorganic nanoparticles is achieved *via* free radical copolymerization. This synthesis method presents several advantages over traditional surface-initiated polymerization techniques, which often rely on controlled polymerization techniques such as RAFT and ATRP. The free radical copolymerization approach can be applied to a wide range of free radical type monomers, while controlled polymerization techniques require a catalyst or initiator that works optimally only for specific monomers or inorganic nanoparticles. Furthermore, due to the affinity of silanes to inorganic materials in general, the present method can also be applied to most inorganic nanoparticles without the need to develop a specific catalyst or initiator for each monomer/inorganic nanoparticle combination. Thus, this approach is generally applicable to diverse nanoparticle/polymer combinations as opposed to the specificity of surface-initiated techniques.
- (2) Although free radical copolymerization yields a wider molecular weight distribution in the grafted polymers, we have shown in this study that this is beneficial for dispersing nanoparticles. In fact, the stabilization effect is the result of a combination of wide molecular weight distribution and high nanoparticle surface curvature. An additional unexplored factor could be that tethering is located along the chain instead of being end-tethered, which cannot be confirmed at present but will be the focus of future studies. As a result of the effectiveness of these stabilization mechanisms, the requirement for a limited range of *P/N* ratios and optimal graft density is relaxed. This allows for a larger design window in the grafted polymer chain length and the amount of polymer grafted onto the nanoparticle in applications.
- (3) We demonstrated that the resultant nanocomposites exhibit concurrently finely tunable functional properties in

refractive index, T_g and bandgap energy. Tunability in multiple functionalities in a melt-processed nanocomposite is highly desirable. In principle, additional functionalities can be introduced simply by incorporating different types of functional nanoparticles, hence expanding the possibilities of functional materials.

- (4) The ability of the nanocomposites to be melt-processable while maintaining the fine dispersion of nanoparticles is particularly attractive for manufacturers. This allows for nanoparticles to be utilized as additives which can be easily added to a base polymer to create novel polymer nanocomposites. The inexpensive and high-throughput melt-blending process potentially allows for more high performance nanocomposites to appear in commercial applications. Some potential applications are optical components requiring tunable refractive index and/or T_g , photoresists with size- or concentration-dependent absorption, dielectric metamaterials, magnetic and piezoelectric-based smart materials, sensors and actuators.

7. Experimental Section

Materials: i) *Materials for Synthesis:* N,N-dimethylformamide (DMF), methanol, and toluene were special grade chemicals purchased from Wako Chemicals. 2,2'-azobisisobutyronitrile (AIBN) and methyl methacrylate (MMA) with 0.005% hydroquinone were Wako special grade chemicals from Wako Chemicals. Zinc acetate dihydrate was special grade and potassium hydroxide was semiconductor grade chemicals purchased from Nacalai Tesque. 3-(Trimethoxysilyl)propyl methacrylate (TSMA) 98% was purchased from Aldrich. Poly(methyl methacrylate) (PMMA) was obtained from Sumitomo Chemicals. The PMMA was analyzed by gel-permeation chromatography using standard polystyrene reference. Number average molecular weight (M_n), weight average molecular weight (M_w) and polydispersity index were found to be 65 kgmol⁻¹, 145 kgmol⁻¹ and 2.241, respectively. MMA was purified through an activated alumina column to remove the inhibitor hydroquinone. All other chemicals were used as received.

ii) *Materials for Elemental Analysis:* Nitric acid was electronic grade, sulfuric acid and hydrochloric acid were Ultrapur grade chemicals and potassium carbonate and sodium carbonate were special grade chemicals purchased from Kanto Chemicals.

Synthesis and Fabrication: i) *Preparation of PMMA-Grafted ZnO Nanoparticles:* The modification of ZnO nanoparticles with TSMA and the subsequent grafting of PMMA has been described in detail in a previous publication.^[30] In brief, a methanol solution of TSMA-ZnO was transferred into DMF, followed by polymerization of MMA with AIBN as initiator under nitrogen atmosphere. Polymerization was carried out for 5 hours at 85 °C and monomer conversion was monitored to ensure completion of the reaction. The nanoparticles were recovered by precipitation in cold methanol. Purification was conducted by dissolving the nanoparticles in toluene and re-precipitation in cold methanol.

ii) *Melt-Blending ZnO/PMMA Nanocomposite:* The PMMA-grafted ZnO batches prepared previously were blended with commercial PMMA to form blended nanocomposite/polymer alloys. Melt-blending was done using a Labo Plastomill from Toyoseiki Co. Ltd., which is a batch-mixer used for homogenizing polymer blends. The ratios of commercial PMMA and PMMA-grafted ZnO, and processing conditions used for preparing each nanocomposite are listed in Supporting Table S2. The blended polymers are subsequently injection-molded into bars of dimensions 63.5 mm × 12.7 mm × 2 mm using a ThermoHaake Injection Molding Unit.

iii) *Annealing of ZnO/PMMA Nanocomposite:* Injection molded nanocomposites were annealed under vacuum for 5 days at 160 °C. The annealed samples were hot-pressed to form 0.20 mm thick sheets

and embedded in epoxy for the preparation of thin sections for TEM observation.

Characterization: i) *Procedure for Cleaving Grafted Polymer from Nanoparticles:* PMMA-grafted ZnO (100 mg) was dissolved in chloroform (4 mL) and Aliquat 336 (10 mg) phase transfer catalyst (a quarternary ammonium salt) was added. 49% HF acid (2 mL) was added to the chloroform solution and the mixture was stirred overnight. Stirring was stopped to allow phase separation, after which the chloroform phase was siphoned off with a polypropylene pipette. The chloroform phase was neutralized by adding saturated sodium bicarbonate solution (4 mL) and shaken vigorously. This procedure was carried out twice, followed by washing with deionized water to remove any remaining ions. The result is a clear solution (5 mL) with a concentration of about 0.017 g mL⁻¹ of solute. The solute contains a majority of cleaved PMMA and the remaining Aliquat 336.

ii) *NMR Characterization of PMMA-Grafted ZnO:* The ²⁹Si solid-state NMR spectra were measured on a Bruker AVANCE 400 spectrometer operating at 79.49 MHz. The ²⁹Si CP/MAS (Cross Polarization with Magic Angle Spinning) experiments were carried out at MAS rates of 4 kHz using densely packed powders of the materials in 7 mm ZrO₂ rotors. The ¹H $\pi/2$ pulse was 4.0 μ s and TPPM (two-pulse phase modulation) decoupling was applied during the acquisition. The Hartmann-Hahn matching condition was optimized at a rotational speed of 4 kHz using polycrystalline tetrakis(trimethylsilyl)silane, which also served as the external chemical shift standard. All spectra were measured with a contact time of 8.0 ms and a relaxation delay of 4 s, and 11284 and 5946 FIDs (Free Induction Decays) were accumulated for Batch 1 and Batch 2, respectively. An exponential multiplication line broadening factor of 100 Hz was applied for the processing of the spectra.

iii) *7.3.3. GPC Determination of Molecular Weight of Grafted Polymer:* Gel permeation chromatography (GPC) was performed on an EcoSEC HLC-8320GPC (TOSOH Bioscience, LLC) equipped with a differential refractometer and UV detector with two TSKgel SuperHM-M 3 μ m, 150 \times 6.0 mm columns connected in series, using the ECOSEC Control (version 1.04, TOSOH Bioscience, LLC) software. The instrument was operated at 40 °C with CHCl₃ as the eluent (flow rate set to 0.60 mL min⁻¹). Polymer solutions were prepared at a known concentration (~2 mg mL⁻¹) and an injection volume of 10 μ L was used. The data was analyzed with ECOSEC Analysis (version 1.04, TOSOH Bioscience, LLC) software with a system calibration curve generated from plotting molecular weight as a function of retention time for a series of broad polydispersity polystyrene standards.

iv) *Elemental Analysis of ZnO/PMMA Nanocomposites:* The zinc oxide and silicon contents of the nanocomposites were determined using Inductively Coupled Plasma Atomic Emission Spectroscopy (ICP-AES) using an ICPS-8100 unit from Shimadzu. The zinc content was first determined then multiplied by a factor of 1.245 (weight ratio of ZnO/Zn) to obtain the ZnO content. Determination of the Zn and Si contents provides information about the amount of silane coupling agents attached to the ZnO surface. The results are listed in Supplementary Table S2. The preparation of analyte solutions for Zn and Si analysis were done separately. Analyte solutions for Zn analysis were prepared in a teflon container using sulfuric acid and nitric acid with microwave digestion using a Milestone MLS-1200 MEGA microwave digestion unit. In the preparation of analyte solutions for Si analysis, nitric acid was added to the samples in a platinum crucible and charred on a hotplate, followed by alkaline fusion using potassium carbonate and sodium carbonate. Subsequent ashing was done in a muffle oven FM-48 from Yamato Scientific. Excess hydrochloric acid was added after ashing to neutralize the analyte solution.

v) *Transmission Electron Microscopy (TEM) of ZnO/PMMA Nanocomposites:* Transmission electron micrographs were obtained on a JEOL JEM-1200Ex and high resolution images were taken with a JEOL JEM 2010. TEM specimens were prepared by cutting nanocomposite samples from the injection-molded bars and ultrathin sections were obtained using an ultramicrotome from Leica Microsystems (EM UC6/FC6).

vi) *UV-Vis Spectrophotometry of ZnO/PMMA Nanocomposites:* UV-Visible transmission spectra were recorded using the Hitachi

U-4100 UV-Vis-NIR spectrophotometer. Standalone film samples were prepared by compression molding at 180 °C and measured for characterizing their transmission properties. Nanocomposites were sandwiched between heated 1 mm thick glass slides and pressed to form a clear film with a thickness of ~0.1 mm. The sandwiched nanocomposites were analyzed with a Shimadzu UV-3600 UV-Vis-NIR spectrophotometer for the absorption spectra. The bandgap energy was determined by characterizing the knee of the absorption edge by taking the intersection of two straight lines extended from the absorption trace before and after the knee. The energy shift was calculated by determining $E_g - E_{g0}$, where E_{g0} and E_g are the bandgap energies of PMMA-g-ZnO dissolved in chloroform and melt-blended in the nanocomposite, respectively. The average measurement of two samples was plotted in the $E_g - E_{g0}$ plot.

vii) *Refractive Index of ZnO/PMMA Nanocomposites:* The refractive index was measured by a prism coupler (Metricon Model 2010) at three wavelengths, 404 nm, 594 nm and 825 nm. Cauchy curve fitting was performed to obtain the refractive index curve from 400 nm to 825 nm. The refractive index at 589.3 nm (sodium D-line) was read from this curve and reported for all samples.

viii) *Dynamic Light Scattering (DLS) of PMMA-Grafted ZnO:* Dynamic light scattering (DLS) measurements were conducted using Delsa Nano C (Beckman Coulter, Inc., Fullerton, CA) equipped with a laser diode operating at 658 nm. Size measurements were made in acetone (refractive index = 1.3575, viscosity = 0.3160 cP at 25 \pm 1 °C). Scattered light was detected at 165° angle and analyzed using a log correlator over 70 accumulations for a 0.7 mL of sample in a glass size cell (0.9 mL capacity). The calculation of the particle size distribution and distribution averages was performed using CONTIN particle size distribution analysis routines. The peak average of histograms from intensity weighted distributions and the z-average diameter out of 70 accumulations was reported as the average diameter of the particles. Five aliquots of 10⁻³ g mL⁻¹ solution prepared from a 10⁻² g mL⁻¹ solution of PMMA-grafted ZnO dispersed in acetone were measured to obtain an average value from five solutions.

ix) *Atomic Force Microscopy (AFM) of PMMA-Grafted ZnO:* Tapping-mode atomic force microscopy was carried out by a Digital Instruments Nanoscope AFM/STM system comprising a Nanoscope II and system controller fitted to a MultiMode TM scanhead. The image was acquired in air using a SuperSharpSilicon SSS-NCL-10 probe (Nanoworld Innovative Technologies; tip radius, cone half angle, nominal force constant and resonance frequency are <2 nm, 10°, 48 N m⁻¹ and 190 kHz, respectively). Highly diluted solutions of nanoparticles were dropped onto a Si wafer cleaned previously by piranha solution. The samples were dried for 3 days at 70 °C before scanning. The lateral particle size was measured and used in the statistical analysis of brush height. To account for tip convolution, which causes a broadening of the lateral dimensions of the scanned particles, a correction was applied using the following equation,^[45] which is valid when the tip radius is small compared to the particle size,

$$r_c = r \left[\cos \theta + \sqrt{\cos^2 \theta + (1 + \sin \theta) \left(\frac{\tan \theta}{\cos \theta} - 1 \right) + \tan^2 \theta} \right] \quad (2)$$

where r_c is the radius of the measured particle size, r is the true radius of the particle and θ is the cone half angle.

Note: Additional information on melt-processing conditions, details of theoretical models and calculations are provided in the Supporting Information. Additional figures including GPC and NMR charts are also provided.

Supporting Information

Supporting Information is available from the Wiley Online Library or from the author.

Acknowledgements

M.W. is grateful to Prof. Karen Wooley for the helpful discussions in the preparation of this manuscript and Phil Imbesi, Ang Li and Sandani Samarajeewa for the assistance with the GPC characterization and Gyu Seong Heo for assistance with DLS. M.W. acknowledges Kaneka Corp for partial funding of this research. J.G. and J.B. thank the National Science Foundation (CHE-0911207, CHE-0840464), The Welch Foundation (A-1706), and the APPEAL Consortium for financial support.

Received: January 11, 2012
Published online: May 23, 2012

- [1] R. D. Tilton, T. Saigal, H. C. Dong, K. Matyjaszewski, *Langmuir* **2010**, 26, 15200.
- [2] a) K. Ohno, K. Koh, Y. Tsujii, T. Fukuda, *Angew. Chem. Int. Ed.* **2003**, 42, 2751; b) M. K. Corbierre, N. S. Cameron, R. B. Lennox, *Langmuir* **2004**, 20, 2867.
- [3] M. A. C. Stuart, W. T. S. Huck, J. Genzer, M. Muller, C. Ober, M. Stamm, G. B. Sukhorukov, I. Szleifer, V. V. Tsukruk, M. Urban, F. Winnik, S. Zauscher, I. Luzinov, S. Minko, *Nat. Mater.* **2010**, 9, 101.
- [4] a) D. Wang, E. W. Edwards, M. Chanana, H. Mohwald, *Angew. Chem. Int. Ed.* **2008**, 47, 320; b) B. P. Binks, R. Murakami, S. P. Armes, S. Fujii, *Angew. Chem. Int. Ed.* **2005**, 44, 4795.
- [5] a) M. Motornov, R. Sheparovych, R. Lupitsky, E. MacWilliams, O. Hoy, I. Luzinov, S. Minko, *Adv. Funct. Mater.* **2007**, 17, 2307; b) B. P. Binks, R. Murakami, S. P. Armes, S. Fujii, *Langmuir* **2006**, 22, 2050; c) E. Katz, M. Motornov, J. Zhou, M. Pita, V. Gopishetty, I. Tokarev, S. Minko, *Nano Lett.* **2008**, 8, 2993.
- [6] Y. Q. Rao, S. Chen, *Macromolecules* **2008**, 41, 4838.
- [7] J. Pyun, S. Jia, T. Kowalewski, G. D. Patterson, K. Matyjaszewski, *Macromolecules* **2003**, 36, 5094.
- [8] D. A. Savin, J. Pyun, G. D. Patterson, T. Kowalewski, K. Matyjaszewski, *J. Polym. Sci., Part B: Polym. Phys.* **2002**, 40, 2667.
- [9] B. Gu, A. Sen, *Macromolecules* **2002**, 35, 8913.
- [10] C. Xu, K. Ohno, V. Ladmira, R. J. Composto, *Polymer* **2008**, 49, 3568.
- [11] a) M. M. Demir, K. Koyunov, U. Akbey, C. Bubeck, I. Park, I. Lieberwirth, G. Wegner, *Macromolecules* **2007**, 40, 1089; b) M. M. Demir, M. Memes, P. Castignolles, G. Wegner, *Macromol. Rapid Commun.* **2006**, 27, 763; c) S. I. Yoo, B. H. Sohn, W. C. Zin, S. J. An, G. C. Yi, *Chem. Commun.* **2004**, 2850.
- [12] R. K. Čapek, M. Weber, A. Eychmüller, *Chem. Mater.* **2010**, 22, 4912.
- [13] L. Meli, A. Arceo, P. F. Green, *Soft Matter* **2009**, 5, 533.
- [14] a) P. G. Degennes, *Macromolecules* **1980**, 13, 1069; b) P. G. Ferreira, A. Ajdari, L. Leibler, *Macromolecules* **1998**, 31, 3994.
- [15] R. Hasegawa, Y. Aoki, M. Doi, *Macromolecules* **1996**, 29, 6656.
- [16] I. Borukhov, L. Leibler, *Macromolecules* **2002**, 35, 5171.
- [17] A. Bansal, H. Yang, C. Li, B. C. Benicewicz, S. K. Kumar, L. S. Schadler, *J. Polym. Sci., Part B: Polym. Phys.* **2006**, 44, 2944.
- [18] C. Chevigny, F. Dalmas, E. Di Cola, D. Gignes, D. Bertin, F. Boue, J. Jestin, *Macromolecules* **2011**, 44, 122.
- [19] P. Akcora, H. Liu, S. K. Kumar, J. Moll, Y. Li, B. C. Benicewicz, L. S. Schadler, D. Acehan, A. Z. Panagiotopoulos, V. Pryamitsyn, V. Ganesan, J. Ilavsky, P. Thiyagarajan, R. H. Colby, J. F. Douglas, *Nat. Mater.* **2009**, 8, 354.
- [20] F. Lo Verso, S. A. Egorov, A. Milchev, K. Binder, *J. Chem. Phys.* **2010**, 133.
- [21] D. M. Trombly, V. Ganesan, *J. Chem. Phys.* **2010**, 133.
- [22] a) Y. Kojima, A. Usuki, M. Kawasumi, A. Okada, Y. Fukushima, T. Kurauchi, O. Kamigaito, *J. Mater. Res.* **1993**, 8, 1185; b) A. Usuki, Y. Kojima, M. Kawasumi, A. Okada, Y. Fukushima, T. Kurauchi, O. Kamigaito, *J. Mater. Res.* **1993**, 8, 1179.
- [23] C. Merckle, J. Blümel, *Chem. Mater.* **2001**, 13, 3617.
- [24] B. Rohe, W. S. Veeman, M. Tausch, *Nanotechnology* **2006**, 17, 277.
- [25] M. Kotecha, W. Veeman, B. Rohe, M. Tausch, *Microporous Mesoporous Mater.* **2006**, 95, 66.
- [26] D. Sun, H.-J. Sue, N. Miyatake, *J. Phys. Chem. C* **2008**, 112, 16002.
- [27] a) C. L. Huang, T. Tassone, K. Woodberry, D. Sunday, D. L. Green, *Langmuir* **2009**, 25, 13351; b) X. W. Fan, L. J. Lin, P. B. Messersmith, *Compos. Sci. Technol.* **2006**, 66, 1198; c) C. Li, J. Han, C. Y. Ryu, B. C. Benicewicz, *Macromolecules* **2006**, 39, 3175; d) W. Ma, H. Otsuka, A. Takahara, *Chem. Commun.* **2011**, 47, 5813.
- [28] a) S. Li, A. Shah, A. J. Hsieh, R. Haghighat, S. S. Praveen, I. Mukherjee, E. Wei, Z. Zhang, Y. Wei, *Polymer* **2007**, 48, 3982; b) R. Palkovits, H. Althues, A. Rumpelcker, B. Tesche, A. Dreier, U. Holle, G. Fink, C. H. Cheng, D. F. Shantz, S. Kaskel, *Langmuir* **2005**, 21, 6048; c) Y. Q. Hu, S. X. Zhou, L. M. Wu, *Polymer* **2009**, 50, 3609; d) J.-Z. Zheng, X.-P. Zhou, X.-L. Xie, Y.-W. Mai, *Nanoscale* **2010**, 2, 2269.
- [29] a) J. Y. Lee, Q. L. Zhang, T. Emrick, A. J. Crosby, *Macromolecules* **2006**, 39, 7392; b) S. Gupta, Q. L. Zhang, T. Emrick, A. C. Balazs, T. P. Russell, *Nat. Mater.* **2006**, 5, 229.
- [30] M. Wong, R. Tsuji, S. Nutt, H. J. Sue, *Soft Matter* **2010**, 6, 4482.
- [31] a) D. Sun, W. N. Everett, M. Wong, H.-J. Sue, N. Miyatake, *Macromolecules* **2009**, 42, 1665; b) M. V. Artemyev, A. I. Bibik, L. I. Gurinovich, S. V. Gaponenko, U. Woggon, *Phys. Rev. B* **1999**, 60, 1504.
- [32] H. Döllefeld, H. Weller, A. Eychmüller, *J. Phys. Chem. B* **2002**, 106, 5604.
- [33] a) P. Rittigstein, R. D. Priestley, L. J. Broadbelt, J. M. Torkelson, *Nat. Mater.* **2007**, 6, 278; b) A. Bansal, H. Yang, C. Li, K. Cho, B. C. Benicewicz, S. K. Kumar, L. S. Schadler, *Nat. Mater.* **2005**, 4, 693.
- [34] a) A. Arceo, L. Meli, P. F. Green, *Nano Lett.* **2008**, 8, 2271; b) H. C. Wong, A. Sanz, J. F. Douglas, J. T. Cabral, *J. Mol. Liq.* **2010**, 153, 79.
- [35] M. Born, E. Wolf, *Principles of optics: electromagnetic theory of propagation, interference and diffraction of light*, Cambridge University Press, Cambridge, New York **1999**.
- [36] T. C. Choy, *Effective medium theory: principles and applications*, Clarendon Press, New York, Oxford **1999**.
- [37] D. R. Lide, *CRC Handbook of Chemistry and Physics*, CRC Press, Boca Raton, FL **1999**.
- [38] Q. Chen, M. R. Lin, J. E. Lee, Q. M. Zhang, S. Yin, *Appl. Phys. Lett.* **2006**, 89, 141121.
- [39] D. Dukes, Y. Li, S. Lewis, B. Benicewicz, L. Schadler, S. K. Kumar, *Macromolecules* **2010**, 43, 1564.
- [40] Y. Tamai, T. Konishi, Y. Einaga, M. Fujii, H. Yamakawa, *Macromolecules* **1990**, 23, 4067.
- [41] W. J. Brittain, S. Minko, *J. Polym. Sci., Part A: Polym. Chem.* **2007**, 45, 3505.
- [42] J. Pyun, T. Kowalewski, K. Matyjaszewski, in *Polymer Brushes*, Wiley-VCH Verlag GmbH, Weinheim, Germany **2005**, 51.
- [43] J. J. Xu, F. Qiu, H. D. Zhang, Y. L. Yang, *J. Polym. Sci., Part B: Polym. Phys.* **2006**, 44, 2811.
- [44] G. D. Smith, D. Bedrov, *Langmuir* **2009**, 25, 11239.
- [45] Technical Manual, NT-MDT, <http://www.ntmdt.com/spm-basics/view/effect-tip-radius-cone-angle>